Anisotropic intergranular damage development and fracture in a 14Cr ferritic ODS steel under high-temperature tension and creep

Hubert Salmon-Legagneur, S. Vincent, J. Garnier, Anne-Françoise Gourgues-Lorenzon, Eric Andrieu

Anisotropic intergranular damage development and fracture in a 14Cr ferritic ODS steel under high-temperature tension and creep

H. Salmon-Legagneur [a,b,c,1], S. Vincent[a,2], J. Garnier[a], A. F. Gourgues-Lorenzon[b*], E. Andrieu[c]

[a]. *CEA Saclay, DEN, DANS, DMN, SRMA, 91191 Gif-sur-Yvette cedex, France*
[b]. *MINES ParisTech, PSL Research University, Centre des Matériaux, UMR CNRS 7633, BP87, 91003 Evry cedex, France*
[c]. *CIRIMAT, ENSIACET, 4 allée Emile Monso, BP44362, 31030 Toulouse, France*

Abstract

This work addresses damage mechanisms at high temperature of a hot extruded 14Cr oxide dispersion strengthened steel rod, in particular, anisotropy induced by its strong morphological and crystallographic texture. Under uniaxial tension, intergranular damage and unstable fracture increased with test temperature; they appeared much easier along the rod axis than perpendicular to it. Creep fracture of smooth specimens involved crack initiation from the side surfaces and intergranular crack propagation, accompanied by intergranular damage.

In order to get rid of fracture surface oxidation by the air environment, a methodology promoting crack nucleation from inside the specimen was built. From tensile and creep tests on notched specimens the fracture initiation location and fracture stability were first mapped as a function of test temperature, maximal stress triaxiality and loading direction. Then, for the first time to the authors' knowledge, interrupted tests on notched tensile and creep specimens, followed by low-temperature fracture allowed revealing fracture surfaces formed at high temperature, but unconnected to the external environment. Intergranular fracture and grain boundary grooving were evidenced there, together with strong chemical reactivity at the surface of internal cavities during damage development at high temperature.

Keywords

Oxide dispersion strengthened ferritic steels; tension; creep; intergranular damage

[1] Now at : Research & Development - Automotive Applications ArcelorMittal Montataire | BP 30109 - 1, route de Saint Leu F-60761 Montataire Cedex, France, email address: hubert.salmonlegagneur@arcelormittal.com
2 Now at : CEA Cadarache, DEN/CAD/DTN/STCP/LCIT Bat. 204, P109, 13108 Saint-Paul Lez Durance Cedex, France
* Corresponding author. Phone +33 1 60 76 30 66; fax +33 1 60 76 31 50. email : anne-francoise.gourgues@mines-paristech.fr

1. Introduction

In future sodium-cooled fast-breeder nuclear reactors, long-term stability of fuel claddings, even at high temperature, is required to insure fuel containment during use and maintenance. Candidate cladding materials should withstand a temperature ranging from 400 to 700°C, and a neutron dose up to 200 displacements per atom leading to 120 to 150 bars of internal pressure at the end of life of the fuel pins due to fission gases production [Yvon and Carré, 2009].

Oxide dispersion strengthened (ODS) steels fabricated from powder metallurgy are currently being considered for these applications. Two chromium contents, namely, 9wt% and 14wt%, have been considered; they respectively lead to a recrystallised martensite and to a fully ferritic microstructure with higher resistance to corrosive products used in fuel disposal procedures. Their development through powder metallurgy manufacturing, their microstructure and current properties have been comprehensively reviewed recently ([Ukai et al., 2017], [Odette, 2018]), so that only essential features are reported in the following. Their body centered cubic matrix ensures good resistance to irradiation induced swelling [A. Alamo et al., 2004]. Their resistance to high temperature viscoplastic flow [A. Alamo et al., 2004] is reached by introducing a high density of fine (Y,Ti,O) precipitates – a few nanometers in size – that mainly form during heating of the mechanically-alloyed powders prior to consolidation (e.g. [Li et al., 2017]). These precipitates are very stable even at high temperature and under irradiation [e.g. Klueh et al. 2005, Sakasegawa et al., 2009]. The chemistry of these nano-oxides, as determined from transmission electron microscopy or from atom probe tomography, may vary with the Y/Ti ratio and precipitate size, whereas their crystal structure is most often consistent with that of $Y_2Ti_2O_7$ pyrochlore (e.g. [Klimiankou et al., 2004], [Ribis et al., 2012], [Zhong et al., 2014]). Their coherency with the matrix may control the high resistance against recrystallisation, which leads to a stable grain structure up to more than 1000°C [Zhong et al., 2014].

Currently developed extruded ferritic 14Cr ODS steels present a bimodal matrix microstructure, with a high proportion of submicron grains (e.g., [Dadé et al., 2016]). This microstructure results from partial abnormal grain growth during the heating stage applied to mechanically-alloyed powders (e.g. [Boulnat et al., 2015], [Sallez et al., 2015]), with strong interaction between the nature of precipitates and the matrix evolution (e.g. [Zhong et al., 2014]). The contribution of various microstructural features such as fine grain size, high dislocation density, high density of nanosized precipitates to the room temperature strength has been recently reassessed [Chauhan et al., 2017].

As for high temperature strength, the high density of grain boundaries allows a good creep resistance under high stresses but several studies reported intergranular fracture of ODS steels, after tensile or creep tests at temperatures higher than 400°C [Steckmeyer et al., 2010] and mainly at 600-650°C ([Wilshire and Lieu, 2004], [Steckmeyer et al. 2012], [Yurechko et al., 2014]). Fracture surface oxidation, however, prevents from fine analysis of the fracture mechanisms. Submicronic particles have been observed inside cavities revealed in polished cross-sections; they that could be either grains or new phases created during cavity development. Nevertheless, one cannot easily rule out possible surface preparation artefacts. Intergranular damage in ODS steels is therefore not fully understood.

The anisotropy in high-temperature mechanical properties of ferritic ODS steels has mostly been reported for tensile tests at 650°C [Ukai et al., 1993, 1] [Ratti, 2009] [Steckmeyer, 2012]. These studies mentioned easier intergranular fracture along the direction of elongated grains than perpendicular to it. The dependence of ductile fracture toughness on the distribution and strengthening efficiency of precipitates has also been investigated up to 550°C [Stradil et al., 2017]. Nevertheless, both high-temperature fracture mechanisms and anisotropy are still scarcely documented in literature, especially for creep tests. Only a few studies reported intergranular damage linked to the so-called “bamboo” grain structure [Ukai et al., 1993, 2], and intergranular damage development in an 18Cr extruded ODS ferritic steel plate [Ratti, 2009].

The aim of this work was to improve current understanding of intergranular damage development in a 14Cr ferritic ODS steel and of the conditions necessary to trigger it, in terms of mechanical loading conditions and of material anisotropy. To this aim, it was thought necessary to reveal damage cavities, unexposed to high-temperature environment, without any metallographic preparation procedure. This was achieved by low-temperature fracture of notched specimens containing internal cracks that had initiated and propagated at high temperature.

2. Material

The investigated material was a Fe-14Cr-1W-0.3Ti-0.3Y_2O_3 (wt. %) ODS ferritic steel produced by powder metallurgy, starting from pre-alloyed 14Cr steel, TiH_2 and Y_2O_3 powders to set the chemical composition. The ratio between yttrium, oxygen and titanium contents was set from a previous optimization work, in order to get a fine distribution of stable nano-precipitates at the end of the whole processing cycle [Ukai et al., 2017], [Chauhan et al., 2017], [Odette, 2018]. High energy ball-milling was followed by hot extrusion at 1150°C and by a 1-hour annealing treatment at 1050°C, leading to a 17-mm-diameter rod [JL Boutard et al., 2014].

The chemical composition shown in Table 1 was determined from a cylinder of Ø12x23 mm^3 taken at the center of this ODS rod. Carbon, excess oxygen and nitrogen mainly originated from the mechanical alloying and consolidation process. Other residuals resulted from atomization of the pre-alloy steel powders.

Table 1. Chemical composition of the investigated ODS steel (wt. %).

Fe	Cr	W	Ti	Y	C	O	N	Al	Mn	Ni	Si	S	P
bal.	13.94	0.95	0.29	0.22	0.025	0.12	0.014	0.010	0.31	0.21	0.27	0.004	0.004

As expected for a hot extruded 14Cr ODS steel [Ukai et al., 1993, 2], the microstructure showed grains elongated along the extrusion direction and standard electron backscatter diffraction (EBSD) analyses (high voltage 15 kV, 50 nm in step size) revealed a strong α-fiber texture, i.e., <110> crystal axes close to the extrusion direction (i.e., the rod axis) (Fig. 1). Perpendicularly to the extrusion direction, the grains were equiaxed and their equivalent circle diameter ranged from 200 nm up to 3 µm, with a mean value of 1.1 µm. Along the extrusion direction (from observation in planes containing both the axial direction, AD, and the radial direction, RD of the rod) the major axis of the grains ranged from 200 nm to 20 µm, with a mean value of 7.6 µm. Coarse, elongated grains with high internal misorientations were found together with smaller, more equiaxed grains, often with crystal orientation off the dominant α-fiber texture component.

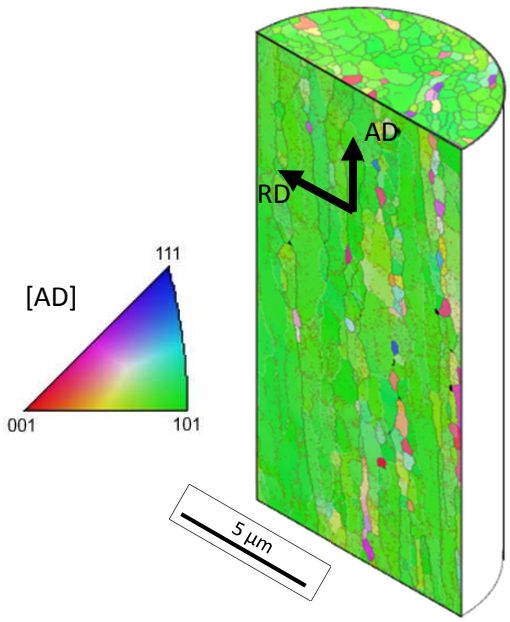

Figure 1. Schematic 3D representation of the anisotropy in grain structure and of crystal orientation of the rod axis (AD) in the crystal frame, from (real) EBSD maps of the as-received ODS steel rod. The <110> α-fiber is represented by green-colored grains.

3. Experimental procedures

3.1. Viscoplastic flow and fracture behavior

Isothermal tensile tests were performed in laboratory air from room temperature up to 850°C. Flat tensile (FT) specimens of 1.5×0.75 mm² gauge section with a 6 mm gauge length, taken along both AD and RD were pulled at prescribed elongation rate of 7×10^{-4} s^{-1}. The load was monitored using a 5 kN cell and the temperature was monitored using two thermocouples, placed on both ends of the specimen. A multi-section radiation furnace was used, with a thermal gradient lower than 5°C. The axial strain in the gauge part was derived from load line displacement measurements, corrected by taking the contribution of load lines and grip systems into account.

Constant load creep tests were performed at 650°C on smooth specimens. Along AD (resp. RD), cylindrical specimens of 4 mm (resp. 2 mm) gauge diameter and 20 (resp. 2.54) mm gauge length were used. Before the tests, the side surface of the specimens was ground down to grade 600 SiC papers to minimize any machining-induced artefacts. The load was gradually applied through a dead weight mechanism with lever arms, at a loading rate of 3 to 5 MPa s^{-1} under monitoring with a 2 kN load cell.

In order to obtain intergranular fracture surfaces unexposed to the external environment, it was necessary (i) to initiate the crack far from any side surface and (ii) to interrupt the test during (stable) crack propagation, so that the effect of specimen geometry on these two phenomena had to be investigated first. To this aim, round U-notched tensile (NT) specimens were used for dedicated tensile and creep tests. Tensile tests on NT specimens first allowed readily determining the critical macroscopic conditions necessary for intergranular damage through a reduced number of tests and simple observations at the macroscopic scale. The geometry of single notched NT specimens was chosen in order to allow machining them along both RD and AD. The diameter of these specimens was 2 mm at notch root and 5 mm away from the notched region. Two notch radii were used. The most severe one (0.4 mm, NT04 specimens) yielded high hydrostatic tension close to the specimen axis; this should promote intergranular microcrack nucleation away from the notch root. The less severe notch root radius (0.8 mm, NT08 specimens) was used to promote stable intergranular cracking and to allow interrupting tests before the crack reached any free surface. The values of the stress triaxiality ratio (of hydrostatic stress to von Mises equivalent stress) at the center of NT specimens were estimated at the end of loading, using a finite element method together with the Cast3M software [Cast3m]; an elastic constitutive assumption yielded values be close to 0.7 and 1.2 for NT08 and NT04 specimens, respectively. Machining such acute U-notches in this hard material appeared difficult, leading to actual notch radii of 0.5±0.1 mm for NT04 and 1.0±0.2 for NT08 specimens, respectively. Consequently, the stress triaxiality ratio was calculated for each specimen according to its actually measured notch geometry.

In order to simplify test interruption right before unstable specimen fracture, double notched tensile (DNT) specimens were also designed, with the same geometry except for a higher total length. The minimum distance between the two (identical) notches that avoided mechanical interaction between them was computed to 4 mm, and thus, the total specimen length (22 mm) prevented from taking these specimens along RD. Consequently, DNT specimens were tested along AD only. To allow interrupting tests in a similar manner along RD, a specific grip was then designed to allow testing two RD-oriented NT specimens in series, i.e., end-to-end (thereafter named End-to-end Notched Tensile specimens, ENT). After interrupting high-temperature tensile or creep tests by fracture of one notch, the specimen half (or the second NT specimen in case of ENT) containing the unbroken notch was pulled up to fracture either inside a liquid nitrogen bath or at room temperature to trigger either cleavage or ductile fracture from unexposed microcracks formed at high temperature.

3.2. Observation of damage development and fracture mechanisms

Fracture surfaces were first observed with a binocular magnifier (BM), in order to investigate local roughness and surface color, which respectively depend on the fracture mechanism and oxidation state (through exposure time

to air). As confirmed with scanning electron microscope (SEM) observations, the brighter parts of the fracture surfaces were strongly oxidized, indicating stable (subcritical) propagation of the crack; less oxidized and tilted (slant) regions resulted from final ductile fracture.

Fracture mechanisms were then identified with field emission gun SEMs (FEG-SEMs); a ZEISS DSM982 Gemini and a FEI Nova NanoSEM 450 were used with a high voltage of 5 to 20 kV and a working distance of 2 to 20 mm according to magnification and spatial resolution required. Fracture surfaces were mostly observed in the secondary electron imaging mode. Damage mechanisms were investigated in polished longitudinal cross sections of broken specimens after a colloidal silica finish, using both secondary and backscattered electron imaging modes. In order to facilitate observations close to fracture surfaces, some specimens were nickel plated before being sectioned.

To investigate the size of grains under ductile fracture surfaces, EBSD mapping was performed using the EDAX TSL OIM software, with a magnification of 5000, a tilt angle of 70°, a working distance of 8 to 18 mm, a voltage of 15 kV, and a hexagonal grid of 50 nm in step size. Acquired data were cleaned up by grain dilation with the following parameters: minimal grain disorientation 5° and minimal grain size of 9 pixels.

4. Results

4.1. Mechanical behavior of smooth specimens

Uniaxial tension behavior

Flat tension specimens exhibited a yield stress and a tensile strength by 50 MPa lower when tested along AD than when tested along RD (Fig. 2a). Ratti explained such yield stress anisotropy by the microstructural anisotropy [Ratti 2009]. FT specimens also presented a lower ductility along RD than along AD, with a fracture elongation by 50 to 70% lower and a reduction of area at fracture by 60 to 70% lower. The observed anisotropy in tensile properties agreed with results reported by [McClintock et al. 2009], [García-Junceda et al., 2012] and [Steckmeyer, 2012].

A maximum in the elongation vs. temperature curves, already known for 14Cr ODS steels [Praud et al., 2012], was observed around 600°C for tensile tests along AD, but not along RD. The reduction of area at fracture was low (around 20%) for tests along RD and rather independent of the test temperature (Fig. 2b).

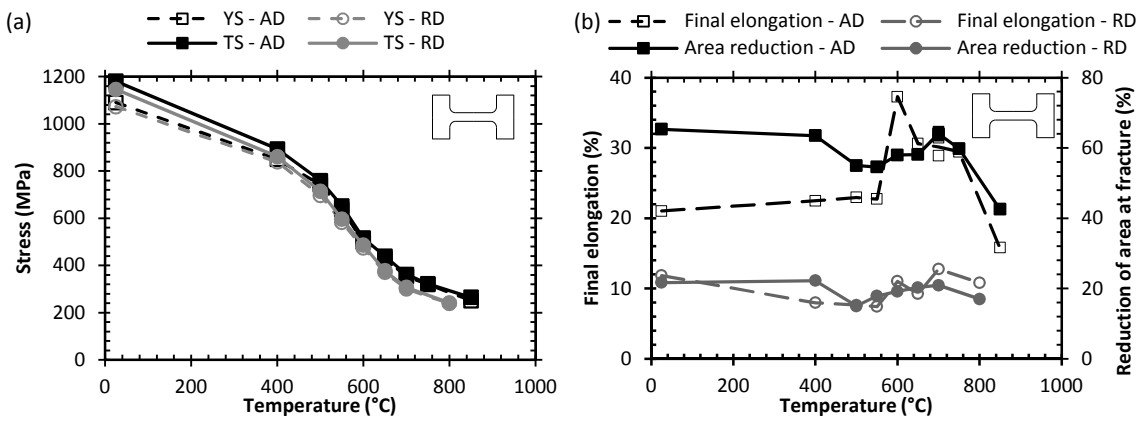

Figure 2. Evolution of (a) yield stress (YS) and tensile strength (TS) and (b) fracture elongation and reduction of area with testing temperature. Inset: specimen geometry.

Creep behavior

For applied stresses lower than 300 MPa, the specimens tested along AD showed a time to rupture 100 times higher than those tested along RD (Fig. 3a), yet with a fracture elongation 2 to 10 times lower. These results are in agreement with those reported by Ratti for an 18Cr ODS ferritic steel rectangular bar [Ratti, 2009]. In the investigated range of stress levels, creep tests along AD evidenced a long primary creep stage with a secondary creep stage (strain rate lower than 10^{-9} h^{-1}) and abrupt rupture right after the onset of tertiary creep, as already reported concerning low stress creep tests on ODS steels (e.g. [Wilshire and Lieu, 2004][Yurechko et al., 2014]). Creep tests along RD led to a short primary creep stage, no steady-state stage but a high amount of strain in the tertiary stage, that is usually representative of high stress creep tests of extruded ODS steels along AD [Ratti, 2009] [Steckmeyer, 2012] (in the present case, 350 MPa).

The Monkman-Grant plot of Fig. 3b revealed that AD and RD specimens exhibiting the same minimum strain rate presented significantly different creep lifetimes, also suggesting anisotropy in deformation and/or fracture mechanism.

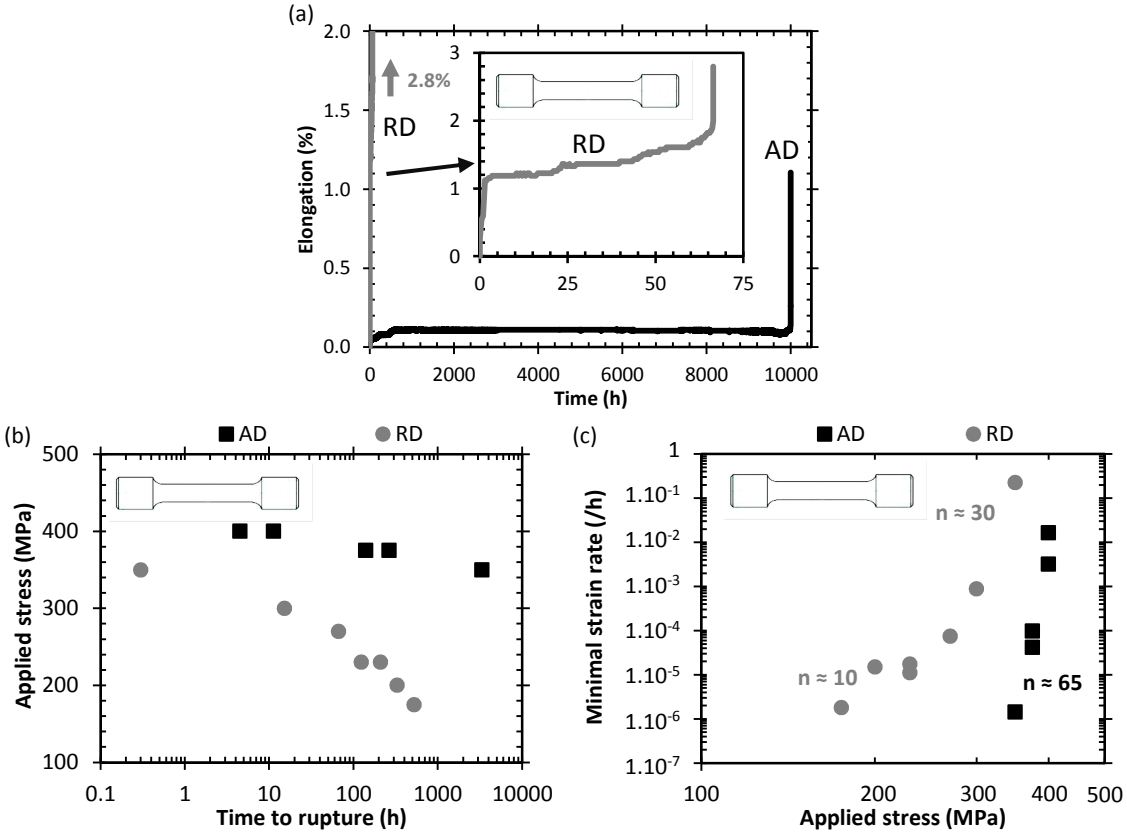

Figure 3. Creep tests results at 650°C on smooth specimens. (a) Creep curves under 270 MPa; (b) Monkman-Grant plot and (c) Norton-like strain rate vs. stress plot.

As already observed from tensile tests, the material shows lower strength and lower ductility along RD than along AD. The apparent Norton power-law exponent n = 65 determined along AD (typically owing to high levels of internal stresses) agreed with reported results on ferritic ODS steels tested along their main elongation/extrusion forming direction [Ratti, 2009; Steckmeyer, 2012]. Along RD, the apparent Norton exponent was much lower and evolved from n = 10 for lower applied stresses (~200 MPa) up to n = 30 for higher applied stresses (> 250 MPa). The differences in power-law exponent along AD and RD might be due to anisotropic levels of internal stresses owing to the material processing route. Their globally high values could be due to interactions between dislocations and nanometer-sized precipitates, as discussed in [Rösler et al., 1992] for nanometer-sized-particle-strengthened aluminum alloys.

4.2. Fracture mechanisms of smooth specimens

Fracture under uniaxial tension

Fracture surfaces of FT specimens tested at 650°C are shown in Fig. 4. These fracture surfaces are similar to those reported in literature [Steckmeyer, 2012]. The specimen tested along AD showed a globally ductile, uniform fracture surface, composed of dimples with particles inside them (Fig. 4b). Particles were rather well separated from each other. Because of their size – a few hundreds of nanometers – these particles could either be oxides formed in the laboratory air after fracture, or smaller grains of the material (see Fig. 1). Yet, from SEM imaging, they seem to be good electronic conductors, so that could indeed indicate that ductile fracture was triggered by some critical amount of intergranular damage development. The fracture surface of FT specimens pulled along RD showed both elongated facets and smaller ones (Fig. 4c), which might again be linked to intergranular fracture.

Fracture surfaces of FT specimens pulled along RD at temperatures above 500°C also showed long strips of larger dimples parallel to AD – up to a few dozen micrometers in width – which could be up to a few hundreds of micrometers in length (Fig. 4d). These strips could also be spotted on specimens tested along AD, through large equiaxed dimples of a few dozen micrometers in width. Inside those dimples, no particle was seen but a few grain boundary facets could be observed. To the authors' knowledge, these strips had not been reported yet in open literature. Observations on cross sections (Fig. 4e) revealed that they were formed in regions of larger grains that originated from abnormal grain growth right before hot extrusion (e.g. [Sallez et al., 2015]).

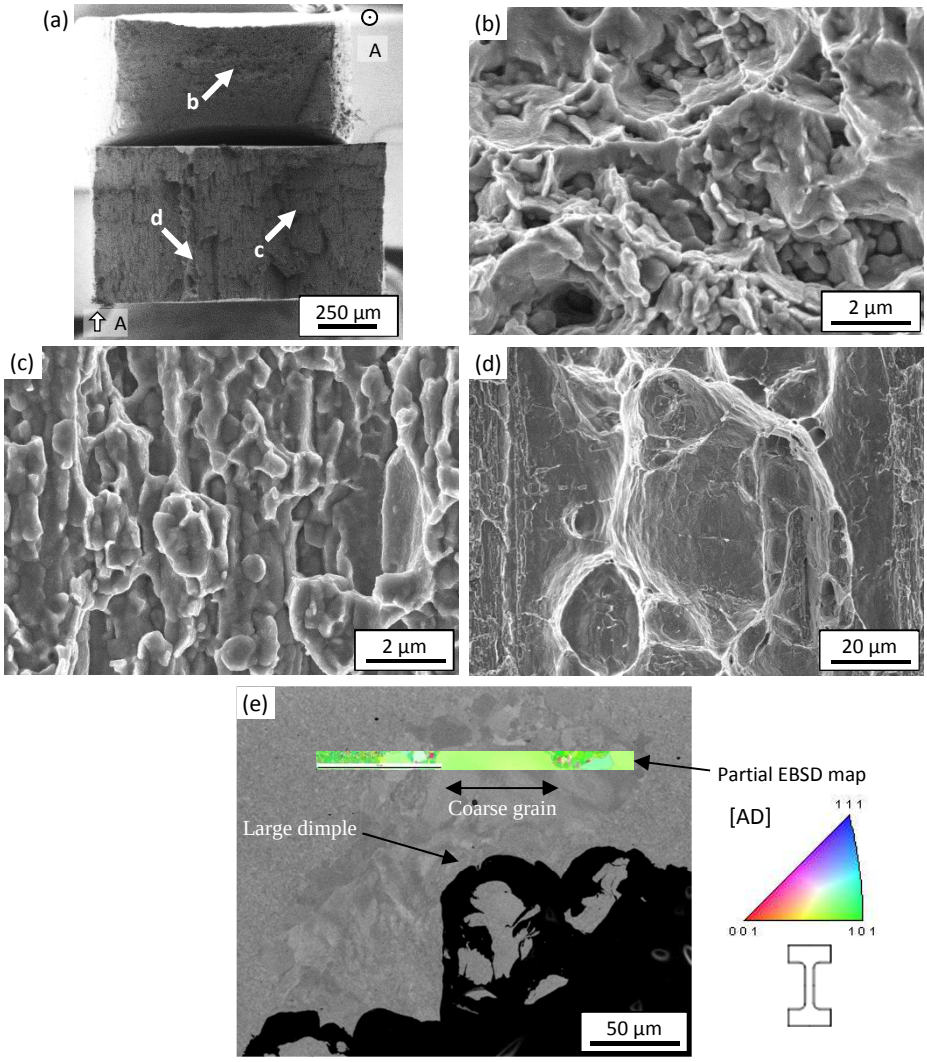

Figure 4. (a) Global view of fracture surfaces of AD and RD FT specimens, pulled at 650°C – 7×10^{-4} s^{-1}, (b) enlarged view of the fracture surface of the AD specimen, (c) and (d) enlarged views of the fracture surface of the RD specimen. (e) cross section under large dimples with superimposed partial EBSD map (color code: orientation of AD in the crystal frame)

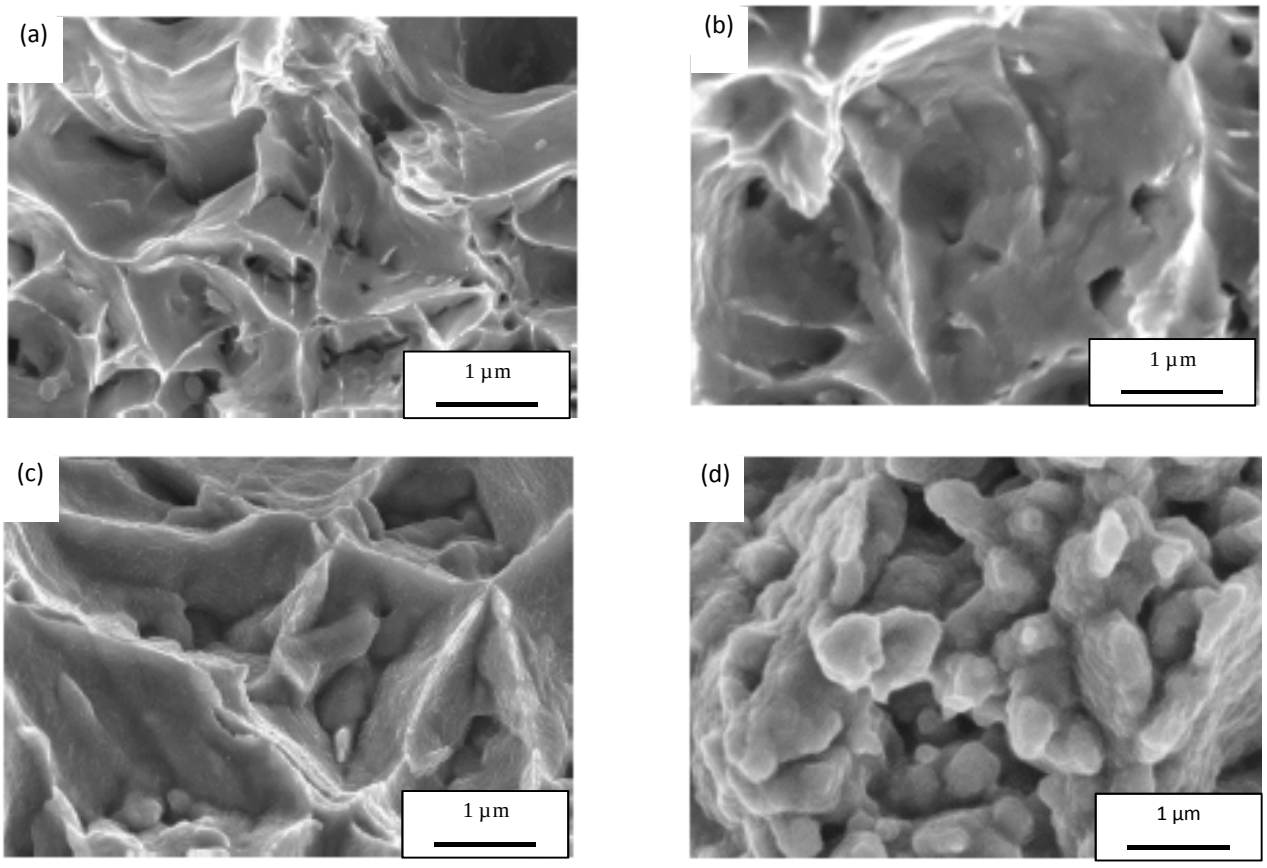

Figure 5. High-magnification views of the fracture surface of FT specimens pulled along AD, at 7×10^{-4} s^{-1}, at (a) 25°C, (b) 400°C, (c) 650°C and (d) 850°C

Detailed views of fracture surfaces of FT specimens pulled along AD revealed an increase in the number of particles found inside the dimples with increasing the test temperature (Fig. 5). At 850°C, dimples almost disappeared and particles covered the whole fracture surface (Fig. 5d). These observations suggest that increasing the test temperature could promote both intergranular damage and surface oxidation after fracture.

Cross-section SEM observations (Fig. 6) showed advanced intergranular damage, with micrometric or sub-micrometric cavities together with larger cavities that probably originated from coalescence of smaller ones. This confirmed that the particles visible on fracture surfaces were indeed grains revealed by intergranular (micro)cracks. In FT specimens, intergranular damage appeared around 600°C, and fracture looked completely intergranular for temperatures higher than 800°C. These results agree with the density increase of particles observed on the fracture surfaces (Fig. 5), further suggesting that these particles were actually grains. The damaged grain boundaries appeared randomly oriented; together with the flat appearance of fracture surfaces (Fig. 5c), this does not confirm the grain boundary sliding mechanism suggested from tensile tests at 10^{-5} s^{-1} by [Ukai et al 1993, 1].

In specimens tested along AD, intergranular microcrack propagation was actually stopped, then followed by ductile tearing (dimples in Fig. 5b). In specimens tested along RD, intergranular crack propagation and coalescence appeared easier, as shown by the absence of noticeable dimples in fracture surfaces (Fig. 4c) and by the lower amount of intergranular damage visible in cross sections. In fact, the individual size of intergranular regions of fracture surfaces (a few micrometers in width but extending across the full sample thickness) was much larger for these specimens than the size of intergranular microcracks (~1 µm) found inside dimples in specimens pulled along AD. When tested along RD, the higher tendency to develop large intergranular cracks could not be compensated by the higher ductility of large coarser-grained regions (evidenced by coarse-dimpled strips) and led to lower macroscopic ductility (Fig. 2b).

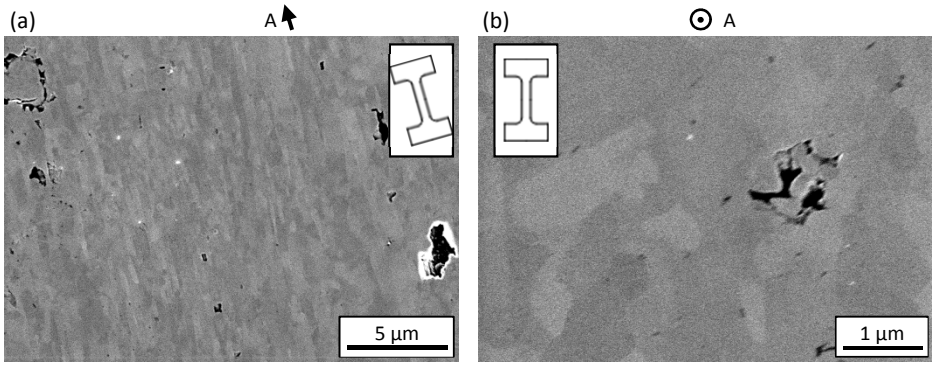

Figure 6. SEM observations of cross sections of FT specimens pulled at 650°C at 7×10^{-4} s^{-1} along (a) AD and (b) RD.

Creep fracture mechanisms

The macroscopic fracture behavior in creep was similar to that in uniaxial tension. Typical fracture surfaces of cylindrical smooth specimens after creep tests are shown in Fig. 7.

The fracture surface of specimens loaded along AD revealed a flat crack together with slant ductile tearing, as shown in Fig. 7a. Flat regions of the fracture surfaces were more oxidized than those of tension specimens, preventing from any observation at finer scale. The less oxidized slant regions showed ductile fracture. The oxidation state of the flat crack probably resulted from long-time exposure to high-temperature air, suggesting a stable crack propagation stage, followed by unstable ductile fracture as soon as a critical stress intensity factor was reached at the tip of the flat crack.

Specimens loaded along RD presented a globally flat but very rough fracture surface (Fig. 7b). From SEM observations, the morphology of the central part of flat regions was similar to that observed after tensile tests along the same direction. The upper and lower parts of the flat region in Fig.7b were strongly oxidized, yet with some appearance of intergranular fracture. The oxidation state of these regions suggested that the cracks initiated from close to the side surfaces of the specimen. These cracks then propagated, probably in a stable manner, across the specimen, and then more quickly joined each other, leading to almost completely flat fracture with only little slant fracture at the end of the test.

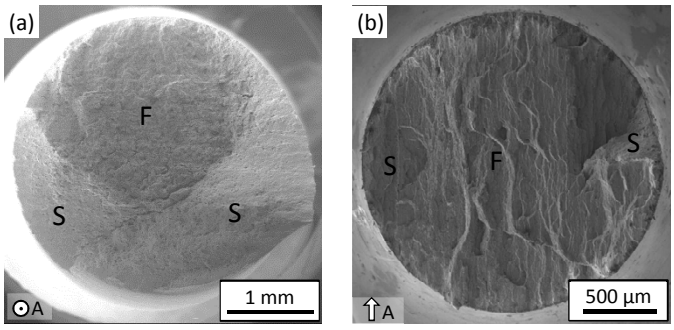

Figure 7. Macroscopic view of typical fracture surfaces of smooth specimens after creep (a) along AD (gauge diameter 4 mm, applied stress 350 MPa, minimum creep rate 9.4×10^{-10} s^{-1}, creep lifetime 417h), and (b) along RD (gauge diameter 2 mm, applied stress 250 MPa, minimum creep rate 1.3×10^{-8} s^{-1}, creep lifetime 140 h). F: flat fracture; S: slant fracture

Typical cross-sections of specimens respectively tested along AD and RD, with a similar time to fracture (a few hundred hours), are shown in Fig. 8. Intergranular damage was present in both specimens under the flat fracture surface, yet with a larger number of cracks and intergranular cavities in the specimen tested along AD. Long cracks

parallel to the loading direction (AD) can be seen in Fig. 8a; they confirm a higher tendency to propagation of intergranular cracks along that direction. Cross-sections of specimens tested along RD revealed a much lower amount of damage (Fig. 8b). This could be due to the easier coalescence of intergranular cavities along AD (here, perpendicular to the loading direction) which lead to earlier fracture, before any extensive development of intergranular damage.

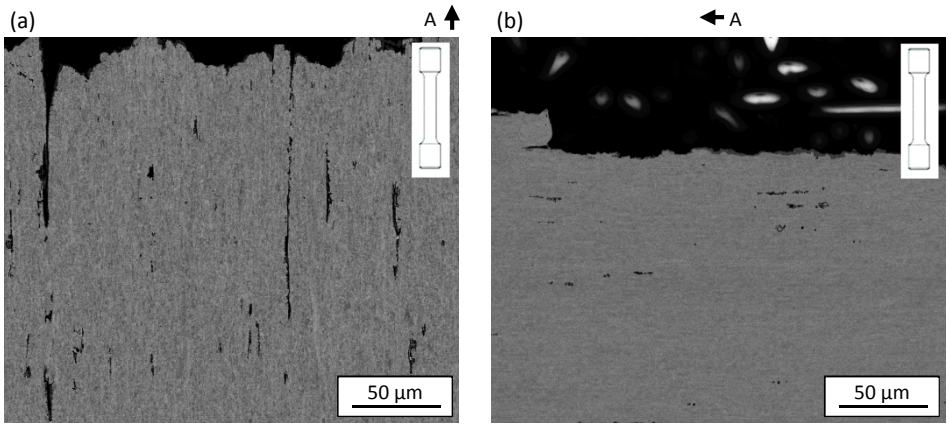

Figure 8. SEM observations of cross sections of smooth creep specimens tested at 650°C (a) along AD under 350MPa (time to rupture 400 h) and (b) along RD under 175 MPa (time to rupture 550 h)

4.3. Macroscopic behavior and fracture mode of notched specimens

The tensile behavior of notched specimens showed an evolution in the location of the stable crack and in global fracture stability with testing temperature, specimen geometry and loading direction (Fig. 9). The maximal load also depended on the loading direction (Table 2). The specimen fracture stability was quantified by measuring the time elapsed between the onset of load decrease (down to 95% of its maximal value) and complete specimen fracture; a critical value of 30 seconds was set as a fracture stability criterion.

The results on FT specimens were also reported in Fig. 9 but the crack initiation location was difficult to analyze on FT specimens pulled along RD (see e.g. Fig. 4a). Only the fracture stability was thus reported in Fig. 9b. For FT specimens pulled along AD, fracture initiated from the center of the specimen at all temperatures; even if small cracks initiated from the side surfaces, they did not propagate enough to lead to final fracture.

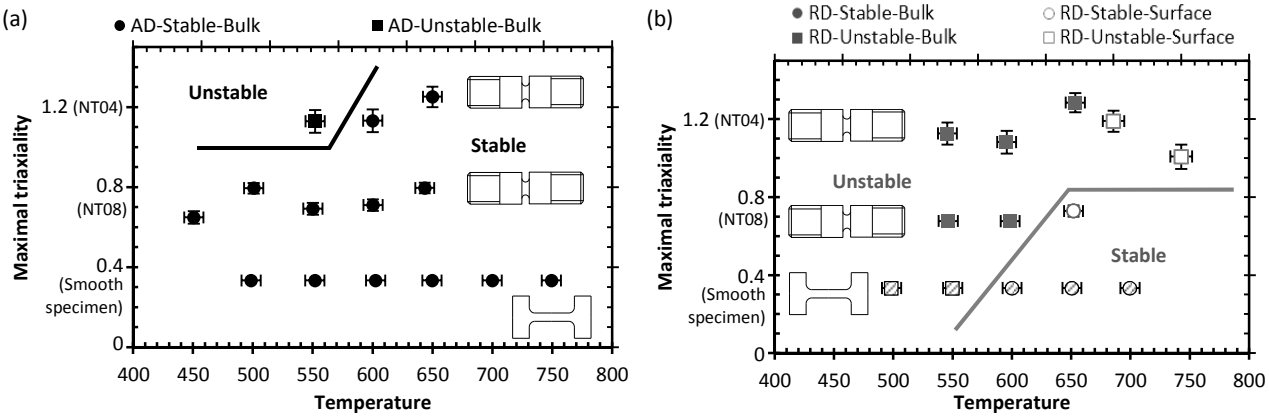

Figure 9. Crack initiation location (from close to the specimen side surface or from the bulk) and global fracture stability during tensile tests, as a function of initial maximal stress triaxiality and test temperature along (a) AD and (b) RD (for which crack initiation location could not be determined in smooth specimens). Lines delineate the boundary between regions of unstable and stable fracture behavior, respectively.

Table 2. Maximal load reached during tensile tests and results of creep tests on notched specimens at 650°C. The creep load has been normalized by the maximum tensile load of a NT specimen of the same geometry, also at 650°C

Loading direction	Specimen geometry	Maximal load (Tensile test) (N)	Normalized creep load	Time to rupture (h)	Fracture initiation location
AD	NT04	1787	80%	44	Bulk
	DNT04		70%	180	Surface
	DNT04		60%	213	Surface
AD	NT08	1671	70%	285	Bulk
	DNT08		70%	442	Surface
	NT08		60%	2075	Surface
RD	ENT04	1461	70%	3	Bulk
	NT04		60%	33	Surface
RD	NT08	1323	70%	37	Bulk
	ENT08		65%	72	Surface
	NT08		60%	62	Surface

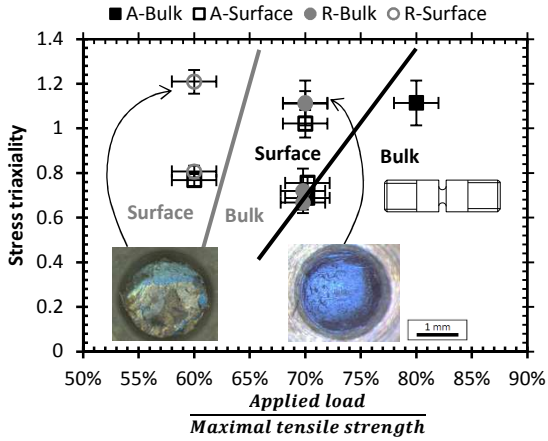

Figure 10. Fracture initiation location as a function of maximal initial stress triaxiality and of normalized applied load during creep tests of NT specimens; the black (resp. grey) line schematically delineates the boundary between fracture initiation from the surface and from the bulk for AD (resp. RD). Typical macrographs (insets) illustrate flat fracture (blue regions) connected to side surfaces

As expected, NT08 specimens exhibited a stronger propensity to stable crack propagation than NT04 specimens. Results also indicate that the crack propagation stability increased with the test temperature. As evidenced by open symbols in Fig. 9, tensile tests revealed a higher tendency of specimens to initiate cracks from the lateral surfaces, even on NT specimens, when tested along RD than along AD. Crack propagation in these specimens also displayed a lower stability (a majority of square symbols is found in Fig. 9b). In smooth tensile specimens, the amount of intergranular damage increased with increasing temperature.

In order to induce slower strains and to trigger intergranular damage for any specimen geometry, creep test loading conditions were set to between 60 and 80% of the maximal load achieved at 650°C in tension for the same specimen geometry and loading direction (Table 2). Under prescribed load, fracture was necessarily unstable. Thus, the flat, strongly oxidized cracks were characterized through BM and SEM observations only in order to locate fracture initiation regions. The results are summarized in Fig. 10.

Creep tests showed that under lower applied load levels, and therefore, under lower strain rates even at the notch root, crack nucleation could occur from the side surface of NT specimens loaded along both AD and RD (Fig. 10). As already observed in tensile tests, the development of intergranular damage close to the notch root then lead to

crack initiation from the side surface of the specimens. As the applied load decreased, the propensity to initiate a stable, intergranular crack from the side surface of NT specimens increased.

4.4. Fracture mechanisms of notched specimens

The fracture surfaces of NT tension and creep specimens revealed strong oxidation of flat surfaces (see the examples in Fig. 10) and signs of intergranular damage, similar to those observed in smooth specimens. Polished cross sections revealed a high amount of intergranular damage cavities, as shown in Fig. 11 for NT04 specimens tested at 650°C along both AD and RD. As for smooth specimens, intergranular damage developed far more extensively in specimens tested along AD (many cavities, frequently aligned parallel to the loading direction) than in specimens tested along RD (cavities or secondary cracks perpendicular to the loading direction). Again, even under high stress triaxiality conditions, intergranular crack propagation appeared easier along AD than along RD.

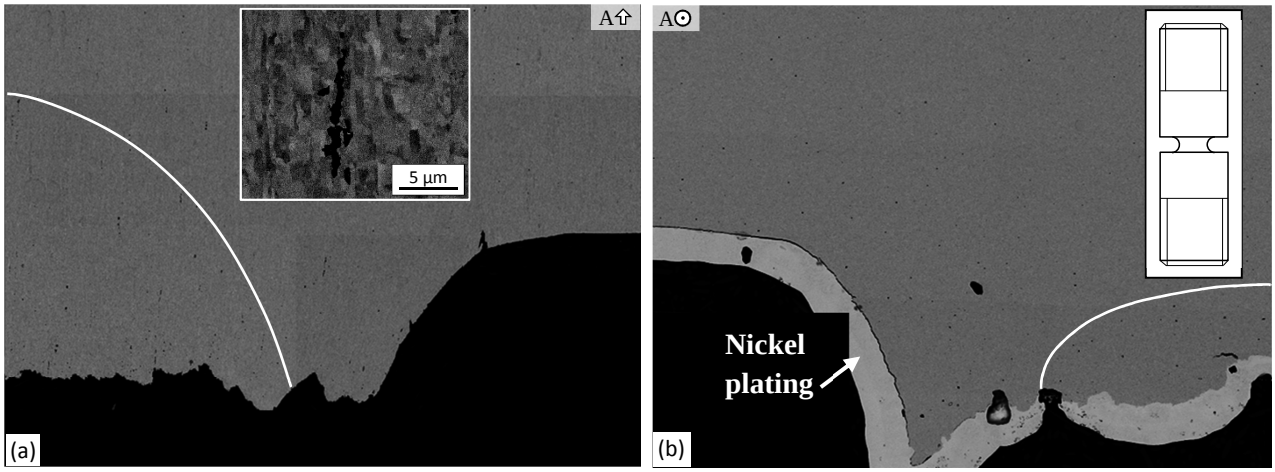

Figure 11. SEM observations of cross section of NT04 specimens tested in tension at 650°C along (a) AD and (b) RD. The white curves delimit the highly intergranular damaged region close to the specimen center from regions with transgranular (ductile) damage or lower amounts of intergranular damage. Insets: (a) detailed BSE image of intergranular damage and (b) schematic view of unbroken NT specimen

4.5. Observation of cavities formed at high temperature but not exposed to the external air environment

Tensile and creep tests on DNT04 and DNT08 specimens followed by cryogenic fracture led to brittle cleavage fracture, with a few regions displaying intergranular-like damage in the fracture surfaces. In fact, no cleavage initiation point was found at the high-temperature damaged regions. By using the size of these zones (around 2 µm, Fig. 12a) and a penny-shape crack assumption, the maximal loads applied during pulling under liquid nitrogen lead to estimate a local stress intensity factor of nearly 2 $MPa.m^{1/2}$. Such a value was too low to trigger crack propagation from the small damaged areas themselves, even at liquid nitrogen temperature. In addition, the size of intergranular cavities was similar to that of many of the cleavage facets, so that the high-temperature damaged regions were difficult to detect on the cleavage fracture surfaces. Nevertheless, up to eight regions were found in each specimen.

Figure 12a presents one of such regions. All these zones exhibited intergranular damage, together with grooved grain boundaries and various types of particles were observed inside them, which could not stem from any metallographic preparation: a distribution of fine particles – a few dozen nanometers in size – (Fig. 12b), some polyhedral, probably crystalline particles (Fig. 12c), and a very thin, fragmented layer on what could be the surface of the grains, i.e., grain boundaries exposed to the internal environment in the cavity (Fig. 12d). Particles in Fig. 12b did not well conduct electrons in the SEM, so that they could possibly be oxides. As already observed in exposed fracture surfaces (e.g. Fig. 5c), grains did not appear close to each other, as if extensive grain boundary grooving would have occurred at high temperature inside the cavity.

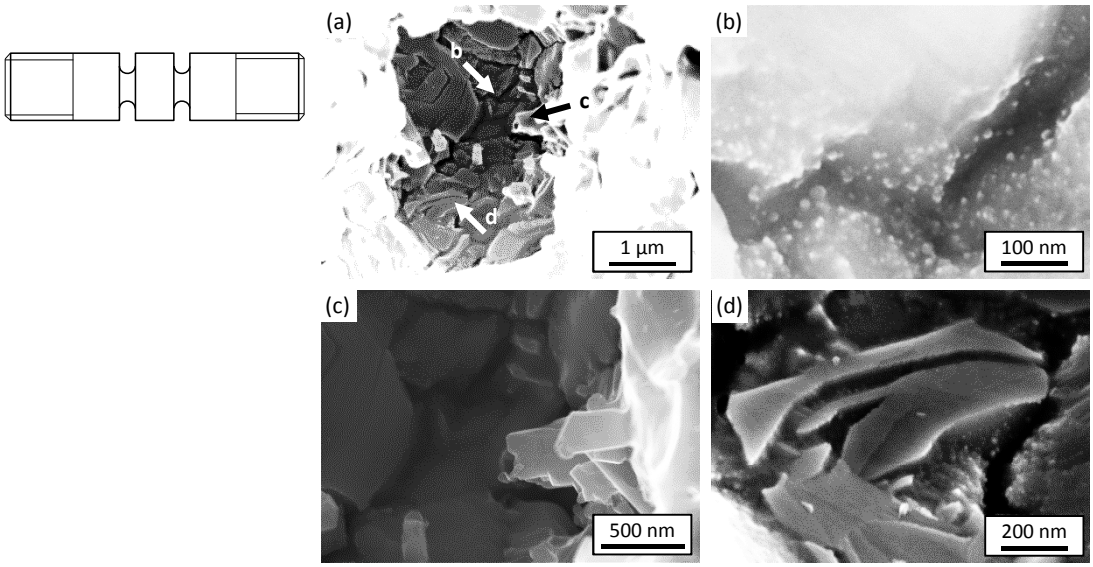

Figure 12. Typical cavity that developed at 650°C in a DNT04 specimen during a tensile test along AD, without connection to the external environment. (a) global view (cavity in dark, surrounding cleavage fracture in bright), and enlarged views of (b) homogeneous dispersion of fine precipitates, (c) small polyhedral particles grown from the cavity surfaces and (d) fragmented layer on the grain boundary surface

In order to reveal a higher number of regions damaged at high temperature, DNT and ENT specimens were also tested in creep (Table 2) in order to increase damage development; the unbroken notch was then fractured by tension at room temperature. For these specimens, dimpled ductile fracture initiated from high-temperature damaged regions that were thus readily found inside the dimples. For such a fine-grained material, this methodology allowed easy observation of more numerous regions damaged at high temperature than the more classical methodology involving brittle failure at low temperature. As shown in Fig. 13, the revealed regions present the same morphology and population of particles as those previously described, suggesting that damage mechanisms were similar under tension (at 7×10^{-4} s^{-1}) and creep, for the investigated range of creep lifetime (up to a few hundred hours).

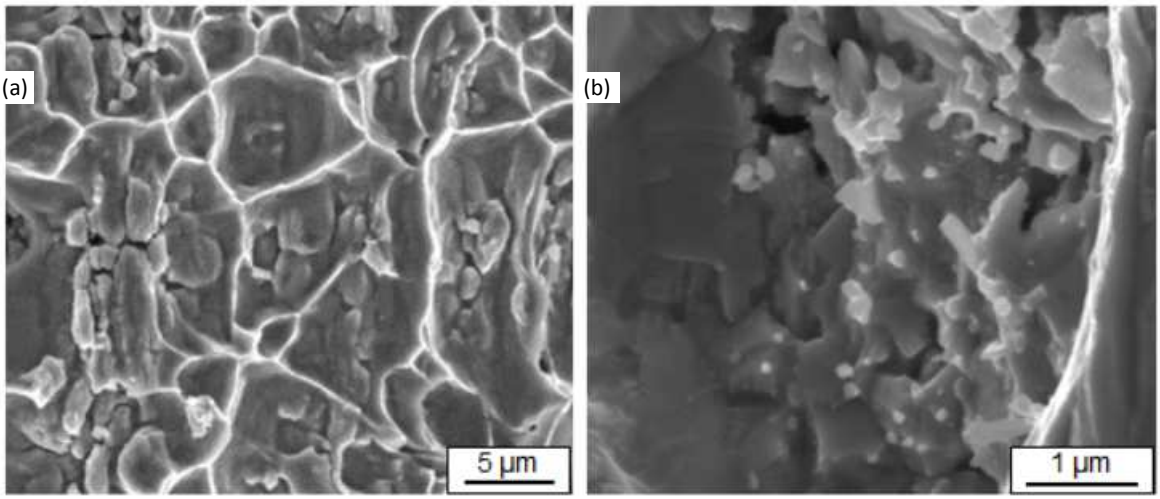

Figure 13. Unexposed intergranular microcracks that developed at 650°C in an ENT specimen creep tested under a net stress (load divided by initial area at notch root) of 270 MPa (lifetime 72h) (a) intergranular fracture inside dimples that were created during final fracture at room temperature and (b) particles typically found in intergranular microcracks

5. Discussion

5.1. Anisotropy in fracture behavior

Whatever the specimen geometry, tensile and creep tests showed shortest lifetime (or lowest ductility) and most limited damage development when the material was loaded along RD. In addition, specimens loaded along RD exhibited lowest strength and most extensive intergranular cracking; whereas those loaded along AD showed extensive coalescence of intergranular cavities along the loading direction (see e.g. Figs 6a, 8a, 11a). Altogether, these results suggest that intergranular crack propagation was much easier and more unstable along RD than along AD. Such anisotropy in crack propagation stability was already reported for a similar 14Cr ODS steel by Fournier et al. on compact tension fracture toughness specimens tested at 600°C [Fournier et al, 2012]. Similar results were obtained in fracture mechanics tests performed during the present work and reported elsewhere [Salmon-Legagneur, 2017]. As many small, equiaxed grains were encountered in the microstructure, the anisotropy in crack propagation could not be directly related to anisotropy in grain boundary density. On the other hand, the presence of coarser, highly elongated grains led to a higher density of *continuous* paths of grain boundaries parallel to the rod axis than perpendicular to it (Fig. 1). More precisely, when loaded along RD, a continuous path of grain boundaries perpendicular to the loading axis, including the boundaries of coarser elongated grains, could easily be found, facilitating propagation of intergranular microcracks. Some of them, involving the boundaries of elongated, coarser grains, are shown in Figs 4c and 13a (fracture surfaces) and in Fig. 8b (in cross-section). On the other hand, elongated grains mainly constituted an obstacle to intergranular propagation perpendicular to AD, so that intergranular microcracks were more readily stopped (see e.g. Figs 4b and 5c).

A possible consequence is that in this material, the creep lifetime of smooth specimens could be driven by their resistance to crack propagation, and not only to instability in viscoplastic flow. Based on these results, a new interpretation of the tertiary creep stage of smooth specimens is proposed as follows.

In smooth creep specimens, the tertiary stage was almost absent in tests along AD; however, stable crack propagation occurred as revealed by the heavily oxidized flat fracture surfaces. Intergranular cracking could even have propagated at the very end of the secondary stage and during the very short tertiary stage, following by ductile fracture. The tertiary stage, in that case, would resemble a fracture toughness test, yet with a low value of fracture toughness even if final fracture was ductile. A rough estimate by using a round bar model, a semi-elliptical crack geometry fitted to the strongly oxidized, flat cracks actually observed and a linear elastic assumption with Mode I loading (as from [Murakami, 1987]) yielded a value between 19 and 34 $MPa.m^{0.5}$ for the fracture toughness of the various smooth creep specimens. This range of values is close to that determined using fracture mechanics specimens also at 650°C [Chaouadi et al., 2010].

When specimens were loaded along RD, the tertiary creep stage involved significant elongation but short amounts of time (Fig. 3a). From fracture surface observations, intergranular cracking nucleated and propagated all across the specimen in two steps: first, in a stable manner (as shown by strongly oxidized regions close to side surfaces, see comment to Fig. 7b), then, in a more unstable manner, leading to less oxidized intergranular facets. As such, at least a part of the quick tertiary stage could stem from crack propagation; if so, crack mouth opening could have contributed to the specimen elongation, in addition to quick viscoplastic strain. In-situ strain field monitoring would help better understanding of the competition between deformation and cracking in the tertiary stage in that case.

5.2 Toward a macroscopic criterion for intergranular fracture

The use of NT specimen geometry allows introducing a gradient in loading conditions inside the specimen. The equivalent stress and strain rate are maximal close to the notch root, whereas for very low amounts of notch

opening (as in the present work), the maximum principal stress and maximum stress triaxiality are located close to the specimen center, together with a very low strain rate. In this material family, it has been shown that a decrease in tensile strain rate leads to an increase in intergranular damage development [Praud et al., 2012], which agrees with the more extended damage development during creep tests than in tensile tests, also noticed in the present work. According to the loading rate of NT specimens, three cases could be encountered:

1. At very high strain rates and/or low test temperatures, all parts of the specimens would fail by ductile tearing.
2. At intermediate loading rates and test temperatures, the notch root would deform "too quickly" to trigger intergranular damage, while the central part could be deformed "sufficiently slowly" to experience intergranular cavitation. The main damage mechanism might therefore be intergranular in the center of the specimen whereas the notch root region would present transgranular ductile damage. This combination of mechanisms leads to crack initiation from the bulk of the specimen. This was the case, in tensile tests, for all specimens tested along AD, and for notched specimens tested along RD at temperatures up to 650°C (Fig. 9).
3. At very low loading rates (e.g., during creep of NT specimens) or very high temperature, all parts of the specimen could be deformed "sufficiently slowly" so that intergranular damage could develop everywhere. The most severely loaded region would now be close to the notch root because of its higher level of strain, so that intergranular cracking would be expected to start from there. This was the case, indeed, for tensile specimens tested along RD at 700 and 750°C (Fig. 9b). It was also the case in NT creep specimens tested at the lowest load levels (see Table 2 and Fig. 10).

In order to set a more quantitative criterion for the transition from case 1 to case 2, a preliminary finite element calculation was performed with the Cast3M software [Cast3m], using a Blackburn flow rule [Blackburn, 1972] and a Von Mises criterion, with constitutive parameters adjusted on creep results of smooth specimens [Salmon-Legagneur, 2017]. A creep test on the NT04 geometry, under a net stress of 325 MPa (normalized load: 70%) along RD was simulated. At the notch root, the estimated strain rate decreased from 1×10^{-4} s^{-1} down to 5×10^{-6} s^{-1} whereas the estimated strain rate in the center of the specimen remained stable, around 1×10^{-6} s^{-1}. The specimen failed from the center (Table 2), indicating that a strain rate of 1×10^{-5} s^{-1} could be a reasonable order of magnitude for triggering intergranular damage at least when pulling in tension along RD. On the other hand, tensile tests at this strain rate led to intergranular fracture, showing that stress triaxiality should not be considered as a first-order parameter in a criterion of intergranular cracking development for this material. The higher stress sensitivity of viscoplastic flow along AD could extend the load (or strain rate) range corresponding to case 2 toward higher values for these specimens, the contrast in strain rate between specimen center and notch root being stronger. This was indeed the case both in tensile tests (initiation from the bulk whatever the temperature, Fig. 9a) and in creep tests (higher critical load to shift toward fracture initiation close to the surface, Fig. 10).

On the other hand, as shear stress and strain rate concentration at the notch root increase with decreasing the specimen notch radius, NT04 specimens could have allowed crack nucleation in the bulk of the material down to lower load levels than NT08, whereas experimental results exhibited the opposite tendency. Grain boundary cavitation was thus not promoted by high tress triaxiality only. This phenomenon suggests that a minimum amount of strain be required to generate intergranular damage. For the sharper notch, the maximal triaxiality inside the specimen was higher and the equivalent shear stress was lower close to the specimen axis. As a consequence, and owing to the high stress dependency of viscoplastic flow (Fig. 3), the amount of strain close to the specimen axis was expected to be much lower at specimen center. It might be not high enough to induce damage development. This was indeed the case: long-lasting creep tests of Table 2 clearly met case 3.

As a whole, tensile and creep tests performed on NT specimens allowed determining a combination of macroscopic conditions – maximal stress triaxiality, temperature, applied load during creep test – necessary for fracture initiation from the bulk and stable crack propagation in the studied material. The strain rate (and corresponding amount of strain) and test temperature seem to be the primary parameters affecting this

phenomenon, whereas stress triaxiality itself only plays a minor role. Moreover, the methodology developed in this work could be extended to other materials that exhibit unstable fracture at high temperature.

5.3. Interactions between grain boundaries and internal (cavity) environment in intergranular cavitation

The presence of grain boundary grooving in cavities revealed after interrupted tests might be attributed either to very small intergranular voids that had coalesced with these cavities, or to displacement of atoms due to some chemical forces (including surface tension) at triple junctions between the cavities and adjacent grains. The presence of non-metallic particles, formed in the cavities but without connection to the external environment, reveal a high chemical reactivity of the (internal) free surfaces freshly created by grain boundary cavitation, with respect to the chemical species that desorbed into the cavity under high uniaxial tension. It also suggests that grain boundary grooving could involve redistribution of atoms along the boundaries. The particle size and location did not allow their chemical analysis; nevertheless, excess carbon, nitrogen or even oxygen solute atoms (see Table 1) in the ferritic matrix could have promoted formation of such non-metallic particles.

On the other hand, the presence of particles and film on the surfaces of intergranular microcracks, even unexposed to the external environment, prevented from finer analysis of the damage mechanism in ODS steels, namely, of the microstructure very close to damaged grain boundaries. In fact, at least the dislocation structure had probably been modified by chemical reactions involving solute atoms during void initiation and growth.

As a consequence, chemical interactions inside the cavities, as well as corresponding atomic fluxes should be further investigated and taken into account in considering the damage development mechanisms: one cannot model high-temperature grain boundary cavitation in this material without considering internal chemical reactions.

6. Conclusions

Tensile and creep tests on smooth and round notched specimens of a 14Cr ferritic ODS steel rod, as well as detailed analysis after fracture or after interrupted tests, led to the following results:

- Intergranular damage was promoted by high temperature (above 500°C), low strain rate ($< 10^{-4}$ s^{-1} along the radial direction at 650°C), and required a minimum amount of viscoplastic strain.
- The strength, ductility and creep lifetime were much lower under loading along the radial direction than under loading along the extrusion direction; this was linked to easier propagation of intergranular cracking along the elongated grains formed during the extrusion process.
- Using notched specimens made it possible to map fracture initiation locus and fracture stability as a function of temperature, loading direction and notch geometry; by using this methodology together with double notched specimens, tensile and creep tests could be interrupted just before final fracture of one notch.
- For the first time to the authors' knowledge, this work revealed intergranular microcracks obtained at high temperature with no connection to the external environment and no specimen metallographic preparation. Microcrack surfaces were covered with non-metallic particles and exhibited grain boundary grooving.
- Strong chemical interactions between cavity walls, surrounding grain boundaries and internal cavity environment cannot be ruled out from the damage development mechanism.

Acknowledgements

The authors wish to acknowledge Agathe Chauvin and Jean-Luc Flament, from CEA Saclay, for the tensile tests, Florent Lefebvre, from CEA Saclay, for his help with the creep tests, Abdennour Meddour, from Mines ParisTech, for the final pulling of DNT/ENT specimens at room temperature and under liquid nitrogen environment and Anne Laurent, from MINES ParisTech, for her help with the EBSD maps.

This work was supported by the joint program "CPR ODISSEE" funded by AREVA, CEA, CNRS, EDF and Mécachrome under contract n°070551.

References

[Alamo et al., 2004] A. Alamo, V. Lambard, X. Averty, M.H. Mathon. **Assessment of ODS-14%Cr ferritic alloy for high temperature applications**, *Journal of Nuclear Materials*, 329-333 A (2004), pp. 333-337. doi: 10.1016/j.jnucmat.2004.05.004

[Blackburn, 1972] L. D. Blackburn, **Isochronous stress–strain curves for austenitic steels,** in : The Generation of isochronous stress–strain curves, ed. A.O. Shaefer, ASME, p. 15-48, 1972.

[Boulnat et al., 2015] X. Boulnat, N. Sallez, M. Dadé, A. Borbély, J.L. Béchade, Y. de Carlan, J. Malaplate, Y. Bréchet, F. De Geuser, A. Deschamps, P. Donnadieu, D. Fabrègue, M. Perez. **Influence of oxide volume fraction on abnormal growth of nanostructured ferritic steels during non-isothermal treatments: An in situ study**, *Acta Materialia*, 97 (2015), pp. 124–130. doi: 10.1016/j.actamat.2015.07.005

[J.-L. Boutard et al., 2014] J.-L. Boutard, V. Badjeck, L. Barguet, C. Barouh, A. Bhattacharya, Y. Colignon, C. Hatzoglou, M. Loyer-Prost, A.L. Rouffié, N. Sallez, H. Salmon-Legagneur, T. Schuler. **Oxide dispersion strengthened ferritic steels: a basic research joint program in France**, *Journal of Nuclear Materials*, 455(1-3) (2014), pp. 605-611. doi: 10.1016/j.jnucmat.2014.08.059

[Cast3M], [online], http://www-cast3m.cea.fr/index.php (as on 3. November, 2017).

[Chaouadi et al. 2010] R. Chaouadi, G. Coen, E. Lucon and V. Massaut, Crack **resistance behavior of ODS and standard 9%Cr-containing steels at high temperature,**Journal of Nuclear Materials, vol. 403 (2010), pp. 15-18. doi: 10.1016/j.jnucmat.2010.05.021

[Chauhan et al., 2017] A. Chauhan, F. Bergner, A. Etienne, J. Aktaa, Y. de Carlan, C. Heintze, D. Litvinov, M. Hernandez-Mayoral, E. Oñorbe, B. Radiguet, A. Ulbricht. **Oxide Microstructure characterization and strengthening mechanisms of oxide dispersion strengthened (ODS) Fe-9%Cr and Fe-14%Cr extruded bars**, *Journal of Nuclear Materials,* 495 (2017), pp. 6-19. doi: 10.1016/j.jnucmat.201707.060

[Dadé et al., 2016] M. Dadé, J. Malaplate, J. Garnier, F. De Geuser, N. Lochet, A. Deschamps. **Influence of consolidation methods on the recrystallization kinetics of a Fe14Cr based ODS steel**, *Journal of Nuclear Materials*, 472 (2016), pp. 143–152. doi: doi.org/10.1016/j.jnucmat.2016.01.019

[Fournier et al., 2012] B. Fournier, A. Steckmeyer, A.-L. Rouffié, J. Malaplate, J. Garnier, M. Ratti, P. Wident, L. Ziolek, I. Tournié, V. Rabeau, J. Gentzbittel, T. Kruml, I. Kubena. **Mechanical behaviour of ferritic ODS steels – Temperature dependancy and anisotropy**, *Journal of Nuclear Materials*, 430(1-3) (2012), pp. 142-149. doi: 10.1016/j.jnucmat.2009.03.024

[A. García-Junceda et al., 2012] A. García-Junceda, M. Hernandez-Mayoral, M. Serrano. **Influence of the microstructure on the tensile and impact properties of a 14Cr ODS steel bar,** *Materials Science & Engineering A*, 556 (2012), pp. 696–703 doi: 10.1016/j.msea.2012.07.051

[Klimiankou et al., 2016] M. Klimiankou, R. Lindau, A. Möslang. **TEM characterization of structure and composition of nanosized ODS particles in reduced activation ferritic-martensitic steels**, *Journal of Nuclear Materials*, 329–333 (2004), pp. 347–351. doi: doi.org/10.1016/j.jnucmat.2004.04.083

[Klueh et al., 2005] R. Klueh, J. Shingledecker, R. Swindeman et D. Hoelzer, **Oxide dispersion-strengthened steels: A comparison of some commercial and experimental alloys,** *Journal of Nuclear Materials*, 341 (2005), pp. 103-114. doi: 10.1016/j.jnucmat.2005.01.017

[Li et al., 2017] W. Li, T. Hao, R. Gao, X. Wang, T. Zhang, Q. Fang, C. Liu, **The effect of Zr, Ti addition on the particle size and microstructure evolution of yttria nanoparticle in ODS steel,** *Powder Technology*, 319 (2017), pp. 172-182. doi: 10.1016/j.powtec.2017.06.041

[McClintock et al., 2009] D. McClintock, M. Sokolov, D. Hoelzer, R. Nanstad. **Mechanical properties of irradiated ODS-Eurofer and nanocluster strengthened 14YWT**, *Journal of Nuclear Materials*, 392(2) (2009), pp. 353-359. doi: 10.1016/j.jnucmat.2009.03.024

[Murakami, 1987] Y. Murakami, "Stress intensity factors handbook", Pergamon Press, 1987.

[Odette, 2018] G.R. Odette. **On the status and prospects for nanostructured ferritic alloys for nuclear fission and fusion application with emphasis on the underlying science**, *Scripta Materialia*, 143 (2018), pp. 142-148. doi: 10.1016/j.scriptamat.2017.06.021

[Praud et al., 2012] M. Praud, F. Mompiou, J. Malaplate, D. Caillard, J. Garnier, A. Steckmeyer, B. Fournier. **Study of the deformation mechanisms in a Fe–14% Cr ODS alloy**, *Journal of Nuclear Materials*, 428 (2012), pp. 90–97. doi: 10.1016/j.jnucmat.2011.10.046

[Ratti, 2009] M. Ratti. **Développement de nouvelles nuances d'aciers ferritiques / martensitiques pour le gainage d'élément combustible des Réacteurs à Neutrons Rapides au sodium**, (Development of new ferritic-

martensitic grades for fuel cladding in sodium-cooled fast-breeder reactors), PhD thesis, Grenoble INP, France (2009) (in French).

[Ribis et al., 2012] J. Ribis, Y. de Carlan. **Interfacial strained structure and orientation relationships of the nanosized oxide particles deduced from elasticity-driven morphology in oxide dispersion strengthened materials**, *Acta Materialia*, 60 (2012), pp. 238–252. doi: 10.1016/j.actamat.2011.09.042

[Rösler et al., 1992] J. Rösler, R. Joos, E. Arzt. **Microstructure and creep properties of dispersion strengthened aluminium alloys**, *Metallurgical Transactions A*, 23(5) (1992), pp. 1521-1539. doi:10.1007/BF02647335

[Sakasegawa et al., 2009] H. Sakasegawa, L. Chaffron, F. Legendre, L. Boulanger, T. Cozzika, M. Brocq, Y. de Carlan **Correlation between chemical composition and size of very small oxide particles in the MA957 ODS ferritic alloy,***Journal of Nuclear Materials*, 384 (2009), pp. 115–118. doi: 10.1016/j.jnucmat.2008.11.001

[Sallez et al., 2015] N. Sallez, X. Boulnat, A. Borbély, J.L. Béchade, D. Fabrègue, M. Perez, Y. de Carlan, L. Hennet, C. Mocuta, D. Thiaudière, Y. Bréchet. **In situ characterization of microstructural instabilities: Recovery, recrystallization and abnormal growth in nanoreinforced steel powder**, *Acta Materialia*, 97 (2015), pp. 377–389. doi: 10.1016/j.actamat.2014.11.051

[Salmon-Legagneur, 2017] H. Salmon-Legagneur. **Caractérisation de l'endommagement à haute température d'aciers ferritiques renforcés par dispersion de nano-oxydes (ODS),** (Characterization of high-temperature damage of ODS ferritic steels), PhD thesis, MINES ParisTech, France (2017) (in French)

[Steckmeyer et al., 2010] A. Steckmeyer, M. Praud, B. Fournier, J. Malaplate, J. Garnier, J.L. Béchade, I. Tournié, A. Tancray, A. Bougault, P. Bonnaillie. **Tensile properties and deformation mechanisms of a 14Cr ODS ferritic steel**, *Journal of Nuclear Materials*, 405 (2010), pp. 95–100. doi: 10.1016/j.jnucmat.2010.07.027

[Steckmeyer et al., 2012] A. Steckmeyer, R. Vargas Hideroa, J.M. Gentzbittel, V. Rabeau, B. Fournier. **Tensile anisotropy and creep properties of a Fe-14CrWTi ODS ferritic steel**, *Journal of Nuclear Materials*, 426 (2012), pp. 182–188. doi: 10.1016/j.jnucmat.2012.03.016

[Steckmeyer, 2012] A. Steckmeyer. **Caractérisation et modélisation du comportement mécanique à haute température des aciers ferritiques renforcés par dispersion d'oxydes,** (Characterization and modelling of high-temperature mechanical behavior of ODS ferritic steels), *PhD*, École nationale supérieure des mines de Paris, (2012). Manuscript (in French) available from https://tel.archives-ouvertes.fr/pastel-00819136/ (as on 3. November, 2017)

[Stradil et al., 2017] L. Stradil, F. Siska, H .Hadraba, D. Bartkova, S. Fintova, V. Puchy, **Fracture behavior of the ODS steels prepared by internal oxidation,** *Fusion Engineering and Design*, 124 (2017), pp. 1108-1111. doi: 10.1016/j.fusengdes.2017.03.008

[Ukai et al., 1993, 1] S. Ukai, M. Harada, H. Okada, M. Inoue, S. Nomura, S. Shikakura, T. Nishida, M. Fujiwara, K. Asabe, **Tube manufacturing and mechanical properties of oxide dispersion strengthened ferritic steel,** *Journal of Nuclear materials*, 204 (1993), pp. 74-80. doi: 10.1016/0022-3115(93)90201-9

[Ukai et al., 1993, 2] S. Ukai, M. Harada, H. Okada, M. Inoue, S. Nomura, S. Shikakura, K. Asabe, T. Nishida, M. Fujiwara. **Alloying design of oxide dispersion strengthened ferritic steel for long-life FBRs core materials**, *Journal of Nuclear Materials*, 204 (1993), pp. 65-73. doi: 10.1016/0022-3115(93)90200-I

[Ukai et al., 2017] S. Ukai, S. Ohtsuka, T. Kaito, Y. de Carlan, J. Ribis, J. Malaplate. **Oxide dispersion-strengthened/ferrite-martensite steels as core materials for Generation IV nuclear reactors,** in: Structural Materials for Generation IV Nuclear Reactors, Elsevier, 2017, Chapter 10, pp. 357-414. doi: 10.1016/B978-0-08-100906-2.00010-0

[Wilshire and Lieu, 2004] B. Wilshire and T.D. Lieu. **Deformation and damage processes during creep of incoloy MA957**. Materials Science and Engineering: A, 386(1-2) (2004), pp. 81-90. doi: 10.1016/j.msea.2004.07.047

[Yurechko et al., 2014] M. Yurechko, C. Schroer, A. Skrypnik, O. Wedemeyer and J. Konys, **Creep-to-rupture of 12Cr- and 14Cr-ODS steels in oxygen-controlled lead and air at 650 °C**, *Journal of Nuclear Materials*, 450(1-3) (2014), pp. 88-98. doi: 10.1016/j.jnucmat.2013.09.063

[Yvon and Carré, 2009] P. Yvon and F. Carré. **Structural materials challenges for advanced reactor systems**, *Journal of Nuclear Materials*, 385(2) (2009), pp. 217-222. doi: 10.1016/j.jnucmat.2008.11.026

[Zhong et al., 2014] S.Y. Zhong, J. Ribis, T. Baudin, N. Lochet, Y. de Carlan, V. Klosek, M.H. Mathon. **The effect of Ti/Y ratio on the recrystallisation behaviour of Fe–14%Cr oxide dispersion-strengthened alloys**, *Journal of Nuclear Materials*, 452 (2014), pp. 359–363. doi: doi.org/10.1016/j.jnucmat.2014.05.033